JGR Space Physics

RESEARCH ARTICLE
10.1029/2022JA031024

Upstream Shift of Generation Region of Whistler-Mode Rising-Tone Emissions in the Magnetosphere

Takeshi Nogi[1] and **Yoshiharu Omura**[1]

[1]Research Institute for Sustainable Humanosphere, Kyoto University, Kyoto, Japan

Key Points:

- The generation region of rising-tone emission below half the cyclotron frequency moves upstream as the frequency increases
- The generation region of a long rising-tone emission moves with a velocity, which is the sum of the resonance velocity and group velocity
- The velocity of the wave packet generation region is controlled by the formation of the resonant current

Correspondence to:
Yoshiharu Omura,
omura@rish.kyoto-u.ac.jp

Citation:
Nogi, T., & Omura, Y. (2023). Upstream shift of generation region of whistler-mode rising-tone emissions in the magnetosphere. *Journal of Geophysical Research: Space Physics*, *128*, e2022JA031024. https://doi.org/10.1029/2022JA031024

Received 17 SEP 2022
Accepted 14 FEB 2023

Author Contributions:
Conceptualization: Takeshi Nogi
Formal analysis: Takeshi Nogi, Yoshiharu Omura
Funding acquisition: Yoshiharu Omura
Methodology: Takeshi Nogi
Software: Takeshi Nogi
Visualization: Takeshi Nogi
Writing – original draft: Takeshi Nogi
Writing – review & editing: Takeshi Nogi, Yoshiharu Omura

Abstract We have performed a series of simulation runs for whistler-mode wave-particle interaction in a parabolic magnetic field with 12 different frequencies of triggering waves and 3 different plasma frequencies specifying cold plasma densities. Under a given plasma condition, a specific frequency range of the triggering wave exists that can generate rising-tone emissions. The generation region of rising-tone emission shifts upstream. The velocity of the wave generation region is dependent on duration of the subpacket, which is controlled by the formation of the resonant current in the generation region. When the source velocity, which is a sum of the resonance and group velocities, is approximately the same as the velocity of the wave generation region, a long-sustaining rising-tone emission is generated. When the spatial and temporal gap between subpackets exists due to damping phase of short subpacket generation, resonant electrons in the gap of the subpackets are carried at the resonance velocity to the upstream region, and the velocity of the wave generation region becomes large in magnitude. When formation of resonant currents is delayed, the velocity of the generation region becomes smaller than the source velocity in magnitude. Below one quarter of the cyclotron frequency, coalescence of subpackets takes place, suppressing formation of the resonant current in the generation region. Since gradual upstream shift of the generation region is necessary for the wave to grow locally, the source velocity should be a small negative value.

Plain Language Summary The generation process of whistler-mode chorus emissions has been a mystery for a long time, while its detailed nonlinear processes are being clarified by particle simulations in recent years. Although it is generally understood that chorus generation regions are close to the magnetic equator, the exact location and process of the wave generation have not been identified yet. It has been observed that a rising-tone chorus emission consists of many subpackets with gradually increasing frequencies. A new subpacket is generated by a foregoing wave packet, and the process is repeated. Instead of the naturally growing wave packet, we inject a wave with a constant frequency to trigger new emissions. We have conducted many simulation runs with different parameters to identify the location and the motion of the generation region. We have found that the generation region always moves upstream from the triggering wave. These characteristics of triggered emissions are valuable information for understanding chorus emissions observed by spacecraft.

1. Introduction

Very low frequency (VLF) triggered emissions are due to generation of new waves with different frequencies from the VLF radio waves transmitted from the ground station (Helliwell, 1967; Helliwell & Katsufrakis, 1974), which is the manifestation of the nonlinear processes (see reviews by Omura et al., 1991 and Gołkowski et al., 2019). The generation of the VLF triggered emissions is controlled by wave-particle interactions in the equatorial magnetosphere when the incident VLF waves propagate along with the geomagnetic field. The wave-particle interaction is also the key driver for generating whistler-mode chorus emissions. Recently, the Demonstration and Science eXperiments (DSX) have been conducted for a study of VLF radio wave transmission from space to space (McCollough et al., 2022; Reid et al., 2022), showing the feasibility and the capability of active experiments in the magnetosphere (McCollough et al., 2022).

Whistler-mode chorus emissions are generated near the equator, growing initially with linear growth rates due to the temperature anisotropy of energetic electrons. A coherent wave grows at a fixed frequency up to a certain level of the wave amplitude (Omura & Nunn, 2011), and new wave packets with varying frequencies are formed through nonlinear wave-particle interaction (Hikishima et al., 2009). Therefore, we can regard chorus emissions with frequency variation as emissions triggered by wave packets naturally growing from thermal fluctuations because of an instability driven by temperature anisotropy of energetic electrons.

The generation mechanism of triggered emissions has been studied for more than half a century. Helliwell (1967) proposed that resonant electrons moving with adiabatic motion generates triggered emissions. Roux and Pellat (1978) have shown that phase space modulation of resonant electrons generates triggered emissions, which are formed by the parallel velocity differences between adiabatic and detrapped electrons. Recently, Tao et al. (2021) proposed Trap-Release-Amplify model, detrapped electrons from the triggering wave generate resonant currents. These models suggest that detrapped resonant electrons are adiabatically transported upstream and generate triggered emissions. Katoh and Omura (2006) showed that resonant currents are generated by the formation of an electron hole in velocity phase space by using an electron hybrid code. Self-consistent particle-in-cell (PIC) simulations of triggered rising-tone emissions also showed that the formation of an electron hole generates resonant currents inducing nonlinear wave growth and frequency increase (Hikishima et al., 2010; Hikishima & Omura, 2012). Nogi and Omura (2022) have introduced the source velocity, which describes an upstream shift of the source region for triggered emissions. We define "upstream" and "downstream" with reference to propagation of waves. Harid et al. (2022) also showed the backward motion of the source region for whistler-mode chorus emissions by an envelope PIC code: However, parametric dependence of the upstream shift remains unclear.

Triggered emissions and chorus waves have subpacket structures (Santolík et al., 2014). Shoji and Omura (2013) have studied the generation models of subpacket structure of ElectroMagnetic Ion cyclotron waves, which have characteristics similar to whistler-mode chorus waves. Hanzelka et al. (2020) have proposed a generation model of subpacket structure for chorus waves. The wave amplitude increases rapidly by the nonlinear wave growth, and phase-organized electrons in the vicinity of the optimum amplitude generate a subsequent subpacket, showing the observation result by Van Allen Probes. Nunn et al. (2021) have shown that triggered emissions with short subpackets are generated from the triggering waves with two different frequencies by using Vlasov Hybrid Simulations. Zhang et al. (2021) have reproduced short rising-tone and falling-tone emissions with high-frequency sweep rate by using four different self-consistent codes. Nogi and Omura (2022) have shown the generation of rising-tone emissions with a long subpacket. The generation process of the subpacket and the duration time of the subpacket remain unclear.

Falling-tone triggered emissions are also generated at the termination of the triggering waves with half the electron cyclotron frequency (Nogi et al., 2020). Generation mechanisms of falling-tone emissions have been studied. Nunn and Omura (2012) have reproduced falling-tone emissions by the Vlasov Hybrid Simulation code, showing the formation of the electron hill. Falling-tone emissions are observed in the termination of the rising-tone triggered emissions when the frequency of the rising-tone emissions exceeds half the electron cyclotron frequency (Nogi & Omura, 2022). The frequency of the triggering waves is an important factor controlling the generation of rising-tone and falling-tone emissions. We conduct simulation runs with different frequencies of the triggering waves. We also change the background plasma frequency, which controls the frequency ranges of wave growth.

Nogi and Omura (2022) presented detailed analyses of a single PIC simulation run reproducing a long subpacket with increasing frequency (Foster et al., 2021), which is triggered by a finite amplitude wave with a constant frequency of $0.3\Omega_e$ under the background plasma density defined by the plasma frequency of $4.0\Omega_e$. They found the generation region moves with the source velocity defined by the sum of the resonance velocity and the group velocity. However, the condition for the long subpacket formation was not clear. In the present study, we analyzed the dependency of the triggering process on the frequency of the triggering wave by changing it from $0.05\Omega_e$ to $0.6\Omega_e$ with an interval of $0.05\Omega_e$. We also studied the triggering process with different plasma frequencies $2.0\Omega_e$ and $6.0\Omega_e$. The series of simulation runs with different parameters shows different processes of generation processes of subpackets forming rising-tone emissions. Simulation methods and parameters are described in Section 2. The simulation results and characteristics of the reproduced triggered emissions are described in the first part of Section 3. Discussions of the generation process of the triggered emissions are given in subsections of Section 3. We give a summary and discussion in Section 4.

2. Simulation Parameters

We conduct PIC simulations by using Kyoto university electromagnetic plasma code (KEMPO) (Omura, 2007; Omura & Matsumoto, 1993). In this paper, our aim is to solve Maxwell's equations and relativistic equations of motion for energetic electrons undergoing cyclotron motion along the magnetic field line near the equator, which requires a code that can resolve nonlinear cyclotron resonant interaction with a time scale of thousands of electron cyclotron periods. KEMPO is a code that allows us to achieve this aim since it has a good property of energy and

Table 1
Simulation Parameters Normalized by Speed of Light c and Equatorial Electron Cyclotron Frequency Ω_e

Parameters	Case 1	Case 2	Case 3
Plasma frequency of cold electrons, ω_p/Ω_e	4.0	6.0	2.0
Grid spacing, $\Delta x/\left(c\Omega_e^{-1}\right)$	0.01	0.01	0.025
Length of simulation region, $L/\left(c\Omega_e^{-1}\right)$	327.68	327.68	819.2
Density ratio of energetic electrons to cold electrons, n_h/n_c	0.01	3.6×10^{-3}	0.01
Thermal momenta of cold electrons, $(u_{c\parallel}/c, u_{c\perp}/c)$	(0.01, 0.01)	(0.01, 0.01)	(0.025, 0.025)
Thermal momenta of energetic electrons at equator, $(u_{h\parallel}/c, u_{h\perp}/c)$	(0.25, 0.30)	(0.25, 0.30)	(0.20, 0.30)
Amplitude of triggering wave, B_{w0}/B_0	6.0×10^{-4}	6.0×10^{-4}	2.0×10^{-4}
Length of damping region, $L_D/\left(c\Omega_e^{-1}\right)$	20.48	20.48	51.2
Coefficient for parabolic magnetic field, $a/\left(c^{-2}\Omega_e^2\right)$	5.0×10^{-6}	5.0×10^{-6}	8.0×10^{-7}

momentum conservation by solving the equations explicitly based on central difference schemes in space and time. We apply a one-dimensional parabolic model of ambient magnetic field for the generation of whistler-mode triggered emissions. We use the same model of background magnetic field as Katoh and Omura (2006). The ambient magnetic field with respect to x is given by $B_0(1 + ax^2)$, while the radial components of the ambient magnetic field are added to the equation of motion, satisfying $\mathrm{div}B = 0$. Rising-tone triggered emissions can be generated when the amplitude of triggering wave is greater than the threshold amplitude (Omura et al., 2009). The wave can grow with an increasing frequency to an amplitude close to the optimum wave amplitude as an absolute instability (Omura, 2021). The optimum amplitude and threshold amplitude are given by

$$\Omega_{\mathrm{op}} = 0.8\pi^{-5/2}\frac{|Q|V_pV_g}{\tau\omega c^2}\frac{U_{\perp 0}}{U_{t\parallel}}\omega_{ph}^2\left(1-\frac{V_R}{V_g}\right)^2\exp\left(-\frac{\gamma^2V_R^2}{2U_{t\parallel}^2}\right), \quad (1)$$

and

$$\Omega_{\mathrm{th}} = \frac{100\pi^3\gamma^4\xi c^7\Omega_e}{\omega\omega_{ph}^4U_{\perp 0}^5\chi^5}\left(\frac{as_2U_{t\parallel}}{Q}\right)^2\exp\left(\frac{\gamma^2V_R^2}{U_{t\parallel}^2}\right), \quad (2)$$

where Q, V_p, V_g, V_R, ω, $U_{\perp 0}$, $U_{t\parallel}$, ω_{ph}, and γ are depth of electron hole, phase velocity, group velocity, resonance velocity, frequency, perpendicular momentum of energetic electrons, parallel momentum of trapped electrons, plasma frequency of energetic electrons, and Lorentz factor, respectively. Parameters ξ and χ are defined from the cold dispersion relation of whistler-mode waves as $\xi^2 = \omega(\Omega_e - \omega)/\omega_p^2$ and $\chi^2 = 1/(1 + \xi^2)$, where ω_p and Ω_e are plasma frequency of cold electron, and electron cyclotron frequency, respectively. The electron cyclotron frequency at the magnetic equator is given by $\Omega_e = eB_0/m_0$, where m_0 is the rest mass of an electron and $-e$ is an electron charge. The phase velocity and the resonance velocity are given by $V_p = c\chi\xi$ and $V_R = [1 - \Omega_e/(\gamma\omega)]V_p$, respectively, where c is speed of light in vacuum. The parameter τ is given by T_N/T_{tr}, where T_N and T_{tr} are the nonlinear transition time to the trapping time necessary for formation of nonlinear resonant current and the trapping time $T_{tr} = 2\pi\sqrt{m_0\gamma/(kV_{\perp 0}eB_w)}/\chi$, respectively. Equations 1 and 2 are calculated for electrons with Maxwellian distribution in the parallel direction. The perpendicular momentum $U_\perp$ in Equations 1 and 2 is an averaged momentum of energetic electrons. The averaged perpendicular momentum for subtracted bi-Maxwellian distribution (Fujiwara et al., 2022) is given by $U_{\perp 0} = U_{t\perp}\sqrt{\pi/2}\left(1 - \beta^{1.5}\right)/(1 - \beta)$, where β and $U_{t\perp}$ are parameters for subtracted Maxwellian distribution assumed in the present simulation.

We have chosen different sets of parameters for three different plasma frequencies. Each set of parameters is determined so that the optimum amplitude is greater than the threshold amplitude over a frequency range of typical rising-tone chorus frequencies. Both threshold amplitude and optimum amplitude are derived under the assumption of an electron hole formed by the resonant electrons in the velocity phase space. We assume depth Q of an electron hole as $Q = 0.5$. The threshold amplitude is obtained by assuming a constant gradient of the wave amplitude for efficient convective wave growth in a parabolic magnetic field given by $B(x) = B_0(1 + ax^2)$, where a is specified in Table 1.

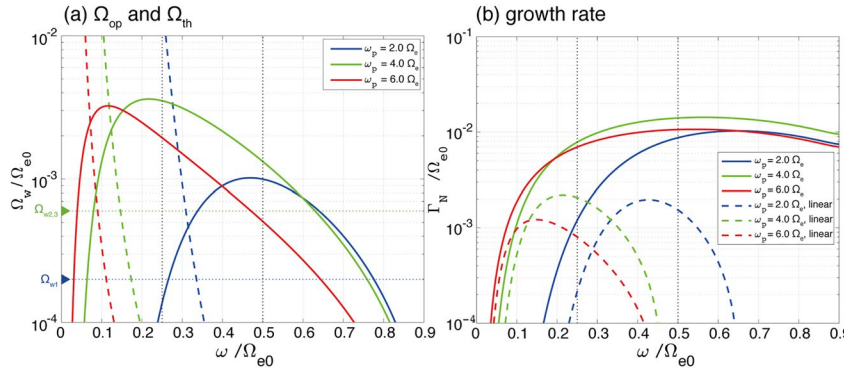

Figure 1. (a) Optimum amplitudes (solid lines), threshold amplitudes (dashed lines), and triggering wave amplitude (triangle marker and dotted lines) for different plasma frequencies $\omega_p = 2.0\Omega_e$, $4.0\Omega_e$, and $6.0\Omega_e$ with $Q = 0.5$ and $\tau = 0.5$ (b) Linear growth rates (dashed lines) and nonlinear growth rates (solid lines) for the optimum amplitudes.

Figure 1a shows optimum and threshold amplitudes at the equator. The frequency band of triggered emissions shifts to the lower frequency ranges as the plasma frequency increases. Both linear growth rate and optimum wave amplitude maximize at lower frequencies with higher plasma frequencies. The nonlinear growth rates for the optimum wave amplitudes are much greater than the linear growth rates, as shown in Figure 1b. The amplitudes of triggering waves are indicated by horizontal dotted lines in blue, green, and red for $\omega_p = 2.0\Omega_e$, $\omega_p = 4.0\Omega_e$ and $6.0\Omega_e$, respectively. When the amplitude of the triggering wave is greater than the threshold wave amplitude, the wave grows to an amplitude around the optimum wave amplitudes. Based on nonlinear theory, nonlinear growth is expected if both of the following conditions are satisfied; The amplitude of triggering wave as a seed wave is greater than the threshold amplitude Ω_{th}, and it is smaller than the optimum amplitude Ω_{op}. We inject triggering waves into the simulation system at the magnetic equator by oscillating two orthogonal external currents with right-handed polarization to the magnetic field. The amplitude of the external current J_{ext} for generating a finite amplitude of magnetic field B_w is obtained by Fujiwara et al. (2022) as $J_{ext} = 2B_w/\mu_0$, where μ_0 is magnetic permeability in a vacuum.

Three different plasma frequencies, $2.0\Omega_e$, $4.0\Omega_e$, and $6.0\Omega_e$ are used in the simulation. Simulation parameters specific for the three cases are shown in Table 1 with normalization by the speed of light c and electron cyclotron frequency Ω_e. Common simulation parameters are shown in Table 2, which are the same parameters as in the simulations by Nogi and Omura (2022). The simulation parameters in Tables 1 and 2 are determined so that linear and nonlinear growth rates are positive over a frequency range. We choose plasma frequency, momenta and density of energetic electron, and amplitude of triggering wave from two conditions. We use a reduced model for the present simulation because of the limitation of computer resource, while the plasma frequency and the density ratio of energetic electrons to cold electrons are set as typical values in the inner magnetosphere with $L = 4$–6. The plasma frequency of the cold electrons in the present study is assumed as $2.0\Omega_e$, $4.0\Omega_e$, and $6.0\Omega_e$. The density ratio of energetic electrons to cold electrons in the present study is in the range from 0.1% to 1% consistent with observations (Juhász et al., 2019; Kubota et al., 2018). The coefficient a for the parabolic magnetic field model is determined so that the critical distance for nonlinear wave growth (Omura et al., 2008) should be in the simulation region. The critical distance is given by

$$h_c = \frac{s_0 \omega \Omega_{u0}}{5 c a s_2 \Omega_{e0}}, \tag{3}$$

where s_0 and s_2 are given by

$$s_0 = \frac{\chi v_\perp}{\xi c} \tag{4}$$

and

$$s_2 = \frac{1}{2\xi\chi}\left\{\frac{\gamma\omega}{\Omega_e}\left(\frac{v_\perp}{c}\right)^2 - \left[2 + \Lambda\frac{\chi^2(\Omega_e - \gamma\omega)}{\Omega_e - \omega}\right]\frac{V_R V_p}{c^2}\right\}. \tag{5}$$

Table 2
Common Simulation Parameters

Parameters	Value
Time step $\Delta t/\Omega_e$	0.0078125
Number of grids	32,768
Total number of cold electrons	1,073,741,824
Total number of energetic electrons	1,073,741,824
Parameters of subtracted Maxwellian distribution ρ, β	1, 0.3
Number of grids for damping region	2,048

By caluclating the critical distance from real parameters $f_{ce} = 7000$ kHz, $\Omega_w = 2 \times 10^{-3}$, $L = 6$ and the plasma frequency for Case 1 ($\omega_p = 4.0\Omega_e$), we obtain the critical distance in latitude as approximately 15°. Nogi and Omura (2022) have shown that the critical distance for rising-tone emission is $75c\Omega_e^{-1}$, and the size of the simulation region is twice as large as the critical distance. Comparing magnetic latitude for the real values with the simulation result (Nogi & Omura, 2022), we obtain the corresponding magnetic latitude in the simulation region in the range from −30° to 30°. Numerical parameters Δx and Δt satisfy the Courant condition (Omura & Matsumoto, 1993) and have sufficient temporal resolution for solving equation of motion with the Buneman-Boris method. Under the parameter Δx, number of grid points in space is sufficient for describing sinusoidal waveform with discrete points. We use absorbing boundaries at both edges of the simulation region with a masking method (Umeda et al., 2001). The size of the absorption region L_D and damping coefficients are the same as those in Nogi and Omura (2022). We set momentum distribution functions for cold electrons and energetic electrons as the bi-Maxwellian distribution and the subtracted bi-Maxwellian distribution, respectively. The ratio of triggering amplitude to the ambient magnetic field is of the order of 10^{-4}.

The amplitude of triggering wave is between the optimum amplitude and the threshold amplitude. The linear growth rate is positive for the frequency range where the nonlinear growth is positive. As we find in Figure 2, the group and resonance velocities are greater in Case 3. We expand the interaction region taken over a longer distance along the magnetic field line for effective wave-particle interaction within the same time scale. Therefore, we have chosen the greater value for the grid spacing to make the system length longer and specified the smaller magnetic field gradient. Nogi and Omura (2022) showed that the source velocity V_S defined by $V_R + V_g$ represents the motion of the triggering points for a new wave packet in Case 1. In Figure 2, we plot V_S in solid lines for $\omega_p = 2.0\Omega_e$, $4.0\Omega_e$, and $6.0\Omega_e$. In the present study, source velocity is defined as the shifts of the wave generation region in a single subpacket, which is given by $V_S = V_g + V_R$ (Nogi & Omura, 2022), and the source region is the area where the single whistler-mode triggered emission is generated. We expand the concept to the multiple subpackets, and we define the wave generation velocity V_W as the shifts of the multiple subpacket generation region. The wave generation region represents the area where the whistler-mode triggered emissions are generated.

3. Results

Figure 3 shows spatial and temporal profiles of magnetic field for forward waves with different triggering wave frequencies from (a) $\omega_0 = 0.05\Omega_e$ to (l) $0.60\Omega_e$ for the plasma frequency $\omega_p = 4.0\Omega_e$. The propagation directions of whistler-mode waves are separated by applying discrete Fourier transformation to B_y and B_z with respect to x. Triggered emissions are observed in the cases of the triggering wave frequency with $0.20\Omega_e$, $0.25\Omega_e$, and $0.30\Omega_e$ in Figures 3d–3f, respectively. Long subpacket structures are observed during the triggered emissions, and the generation region of triggered emissions shifts upstream. Figures 4a–4l show spatial and temporal profiles of instantaneous frequencies for forward propagating triggered emissions for the plasma frequency $\omega_p = 4.0\Omega_e$. We separate triggered emissions from triggering waves by applying discrete Fourier transformation with respect to time. Instantaneous frequency is calculated by the inverse of the period of the wave phase of magnetic fields from $-\pi$ to π. In Figure 4, we plot instantaneous frequencies for triggered emissions with amplitudes greater than 6.0×10^{-4} of the equatorial background magnetic field. We find that triggered emissions in Figures 4d–4f are rising-tone emissions. The instantaneous frequency of those cases smoothly increases from the frequency of triggering waves.

Figure 5 shows spatial and temporal profiles of magnetic field for forward waves with different triggering wave frequencies from (a) $\omega_0 = 0.05\Omega_e$ to (l) $0.60\Omega_e$ for the plasma frequency $\omega_p = 6.0\Omega_e$. Triggered emissions are observed in the cases of the triggering wave frequency with $0.15\Omega_e$ and $0.20\Omega_e$ in Figures 5c and 5d. A shorter subpacket is generated repeatedly, and the generation region of the subpackets moves upstream. Figures 6a–6l show spatial and temporal profiles of instantaneous frequency for forward propagating triggered emissions for the plasma frequency $\omega_p = 6.0\Omega_e$. We find that triggered emissions in Figures 5c and 5d are rising-tone emissions. The instantaneous frequencies of these cases smoothly increase from the frequencies of the triggering waves.

Figure 7 shows spatial and temporal profiles of magnetic fields of forward waves with different triggering wave frequencies from (a) $\omega_0 = 0.05\Omega_e$ to (l) $0.60\Omega_e$ for the plasma frequency $\omega_p = 2.0\Omega_e$. In the cases of the triggering wave frequency from $0.35\Omega_e$ to $0.50\Omega_e$, we observe triggered emissions as shown in Figures 7g–7j. Comparing Figure 7 with Figure 3, we find that shorter subpackets are intermittently generated, but the generation region

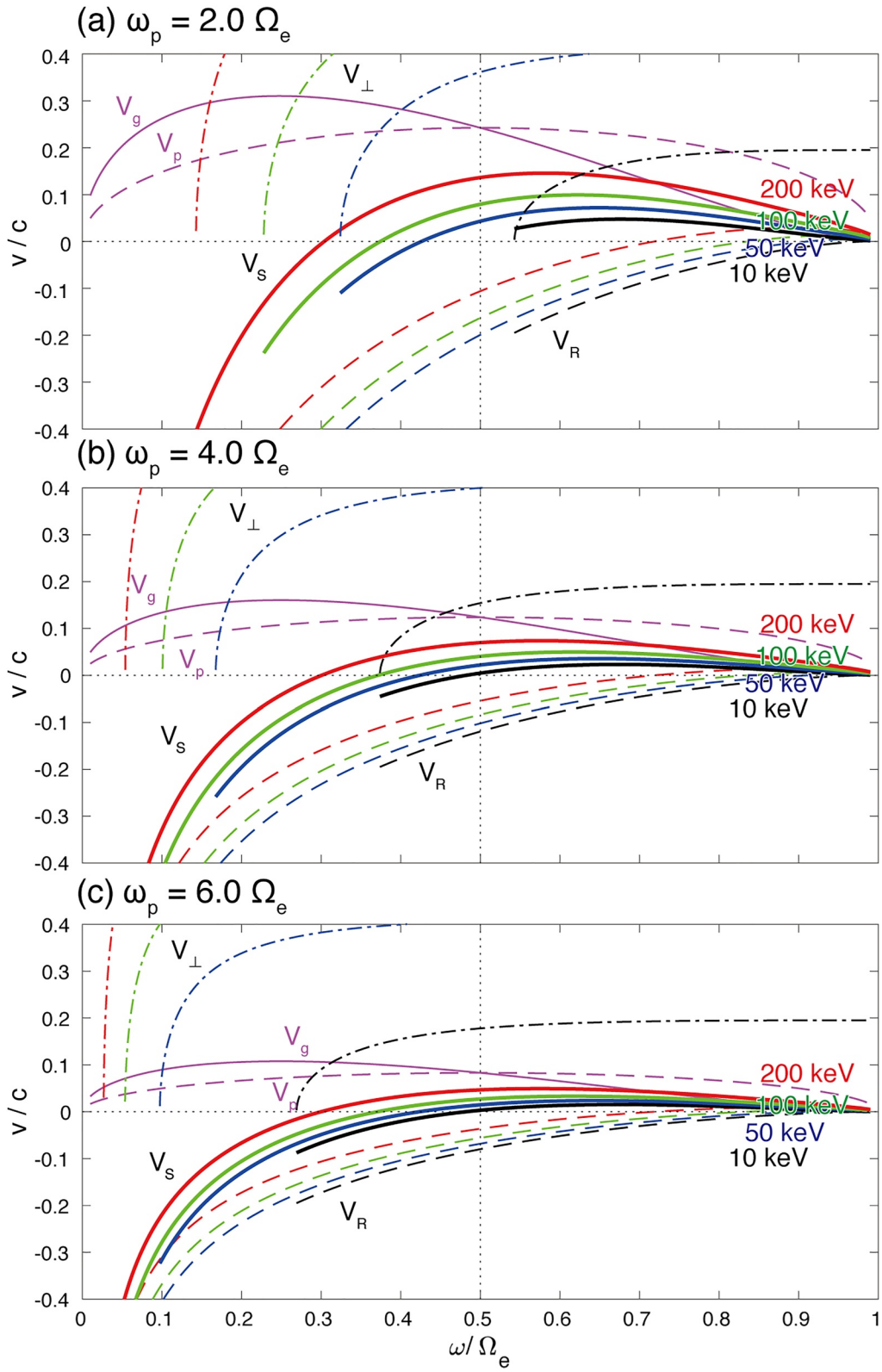

Figure 2. Group velocity V_g, phase velocity v_p, resonance velocities V_R, perpendicular velocities $v_\perp$, and source velocity V_S as functions of frequency for 10, 50, 100, and 200 keV electrons with plasma frequencies (a) $\omega_p = 2.0\Omega_e$, (b) $4.0\Omega_e$, and (c) $6.0\Omega_e$, respectively.

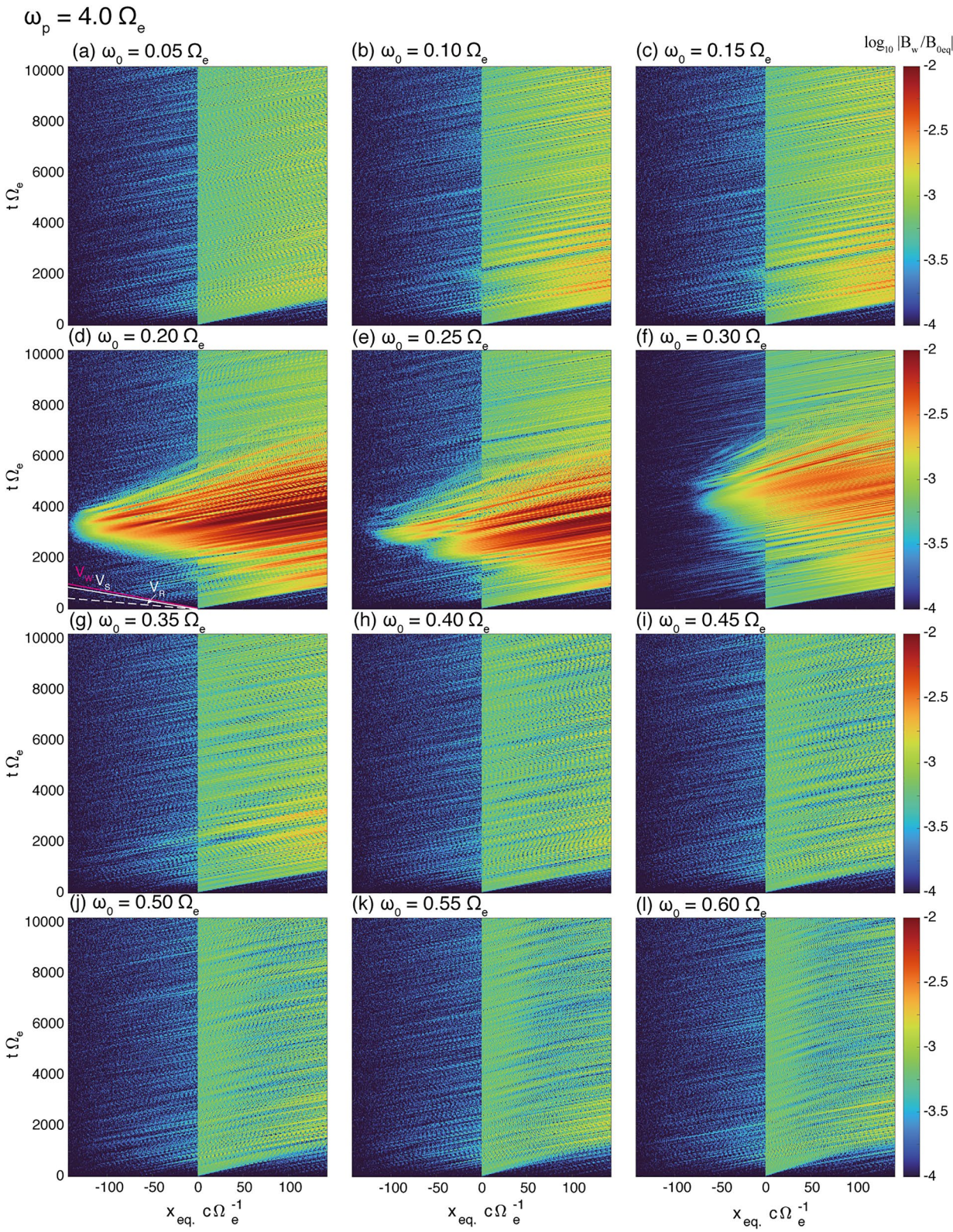

Figure 3. Spatial and temporal profiles of magnetic fields for forward waves for Case 1 with plasma frequency $\omega_p = 4.0\Omega_e$ and triggering wave frequencies ω_0 from (a) $0.05\Omega_e$ to (l) $0.60\Omega_e$, respectively. (d) (solid magenta line) The velocity of wave generation V_W, (dashed white line) the resonance velocity for 100 keV electrons at the magnetic equator, (solid white line) the source velocity V_S for 100 keV electrons at magnetic equator.

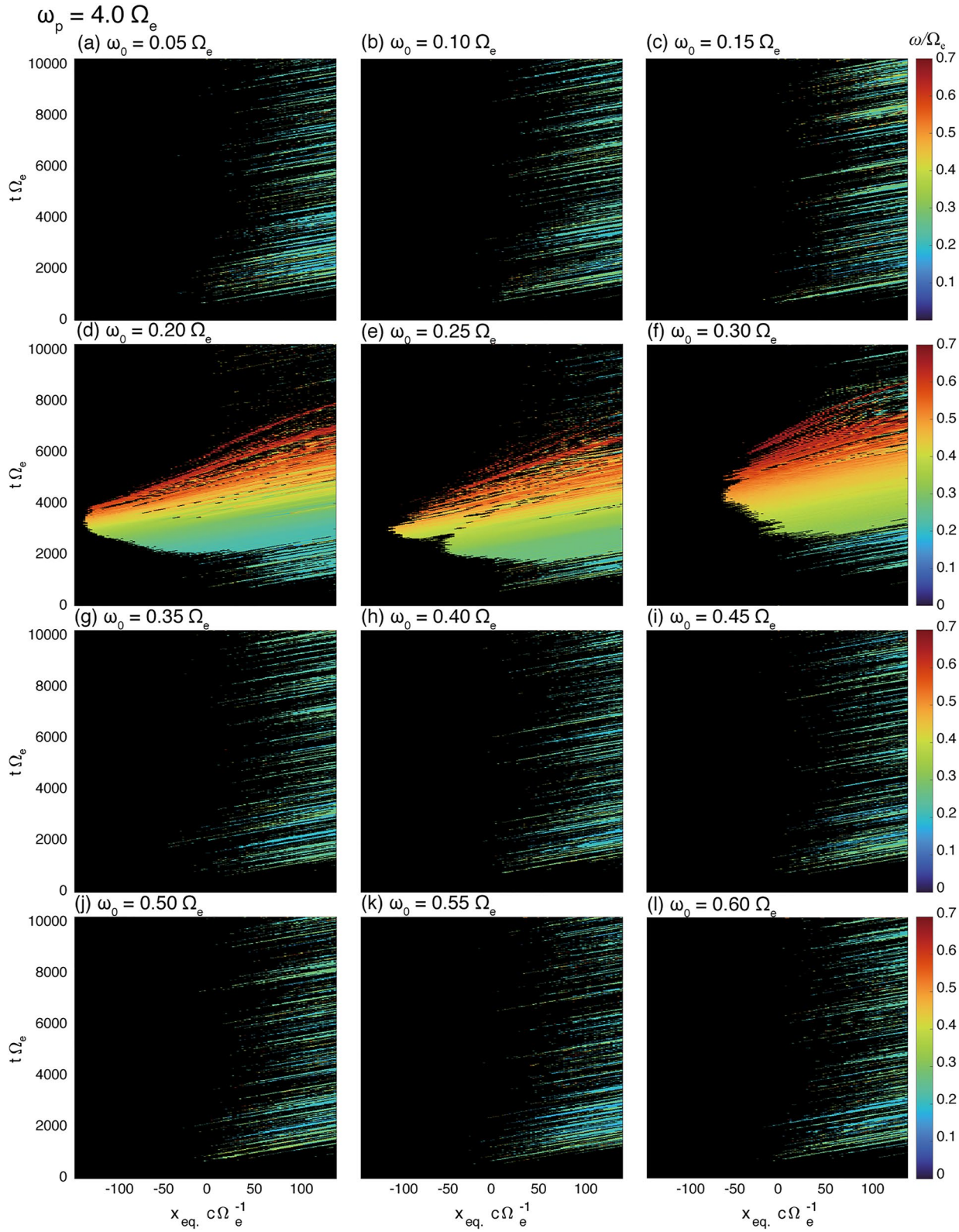

Figure 4. Spatial and temporal profiles of instantaneous frequency of triggered emissions for Case 1 with the plasma frequency $\omega_p = 4.0\Omega_e$ and different triggering wave frequencies ω_0 (a) $0.05\Omega_e$ to (l) $0.60\Omega_e$, respectively.

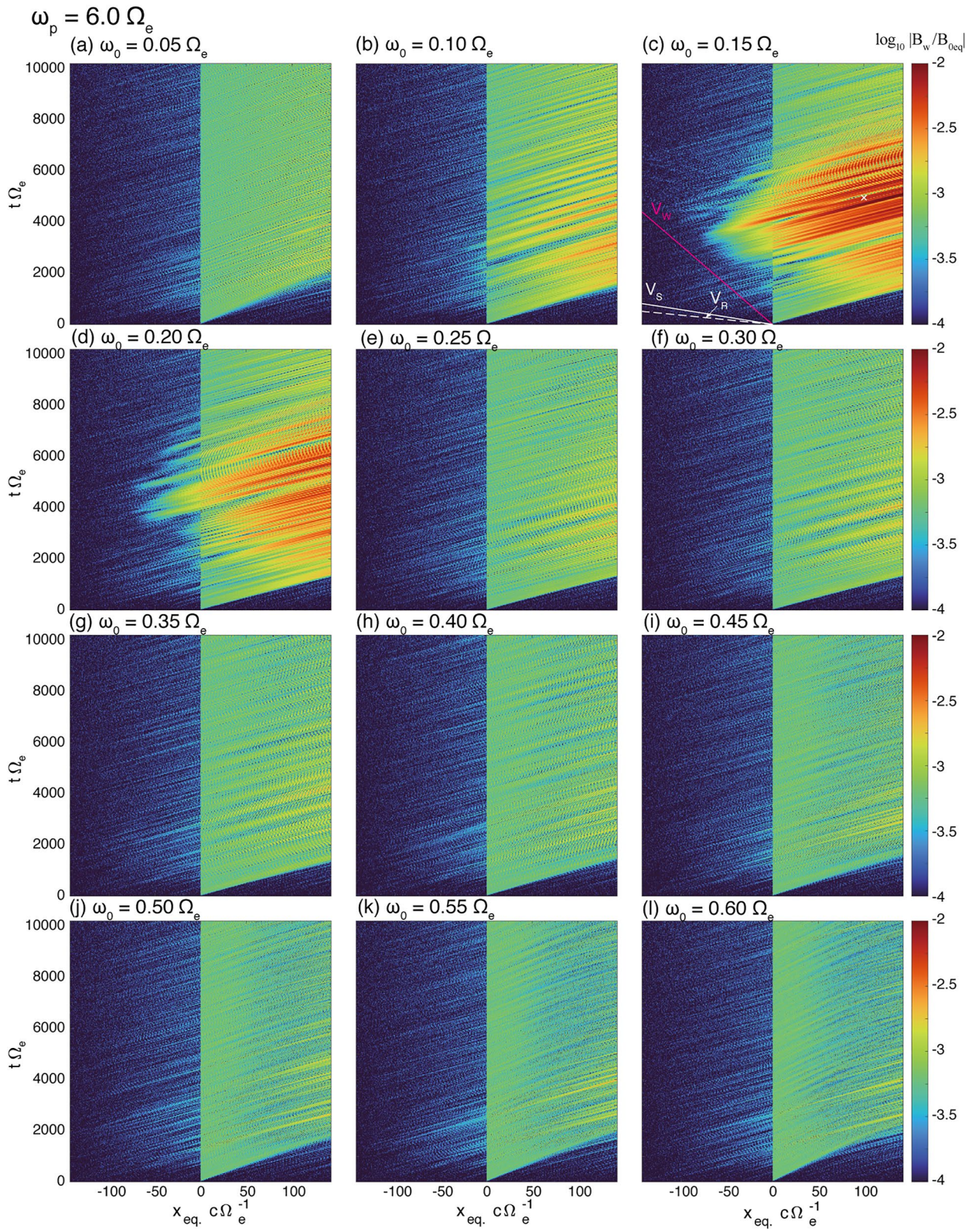

Figure 5. Spatial and temporal profiles of magnetic fields for forward waves for Case 2 with plasma frequency $\omega_p = 6.0\Omega_e$ and triggering wave frequencies ω_0 from (a) $0.05\Omega_e$ to (l) $0.60\Omega_e$, respectively. (c) (solid magenta line) The velocity of wave generation V_W, (dashed white line) the resonance velocity for 100 keV electrons at the magnetic equator, (solid white line) the source velocity V_S for 100 keV electrons at the magnetic equator.

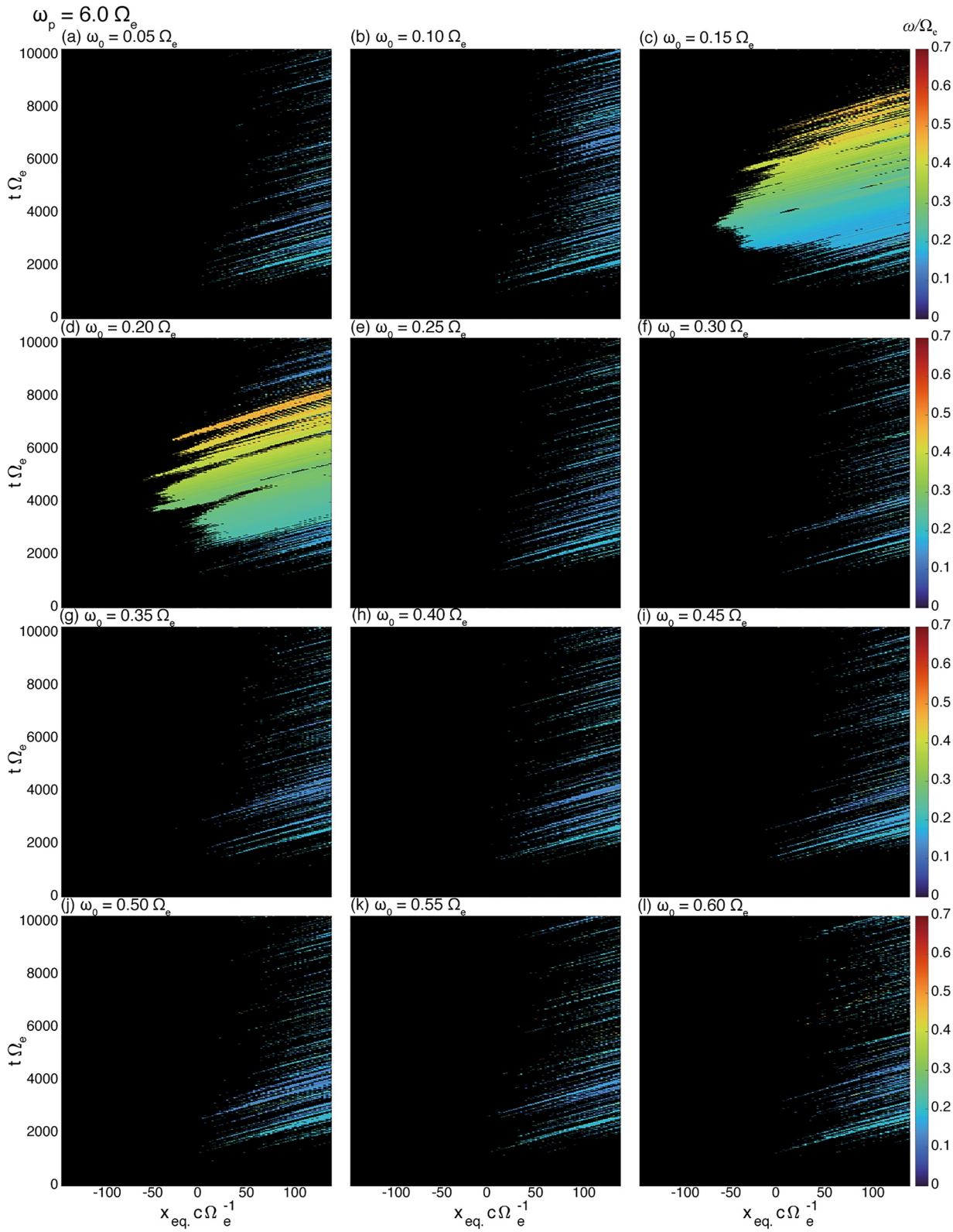

Figure 6. Spatial and temporal profiles of instantaneous frequency of triggered emissions for Case 2 with the plasma frequency $\omega_p = 6.0\Omega_e$ and different triggering wave frequencies ω_0 from (a) $0.05\Omega_e$ to (l) $0.60\Omega_e$, respectively.

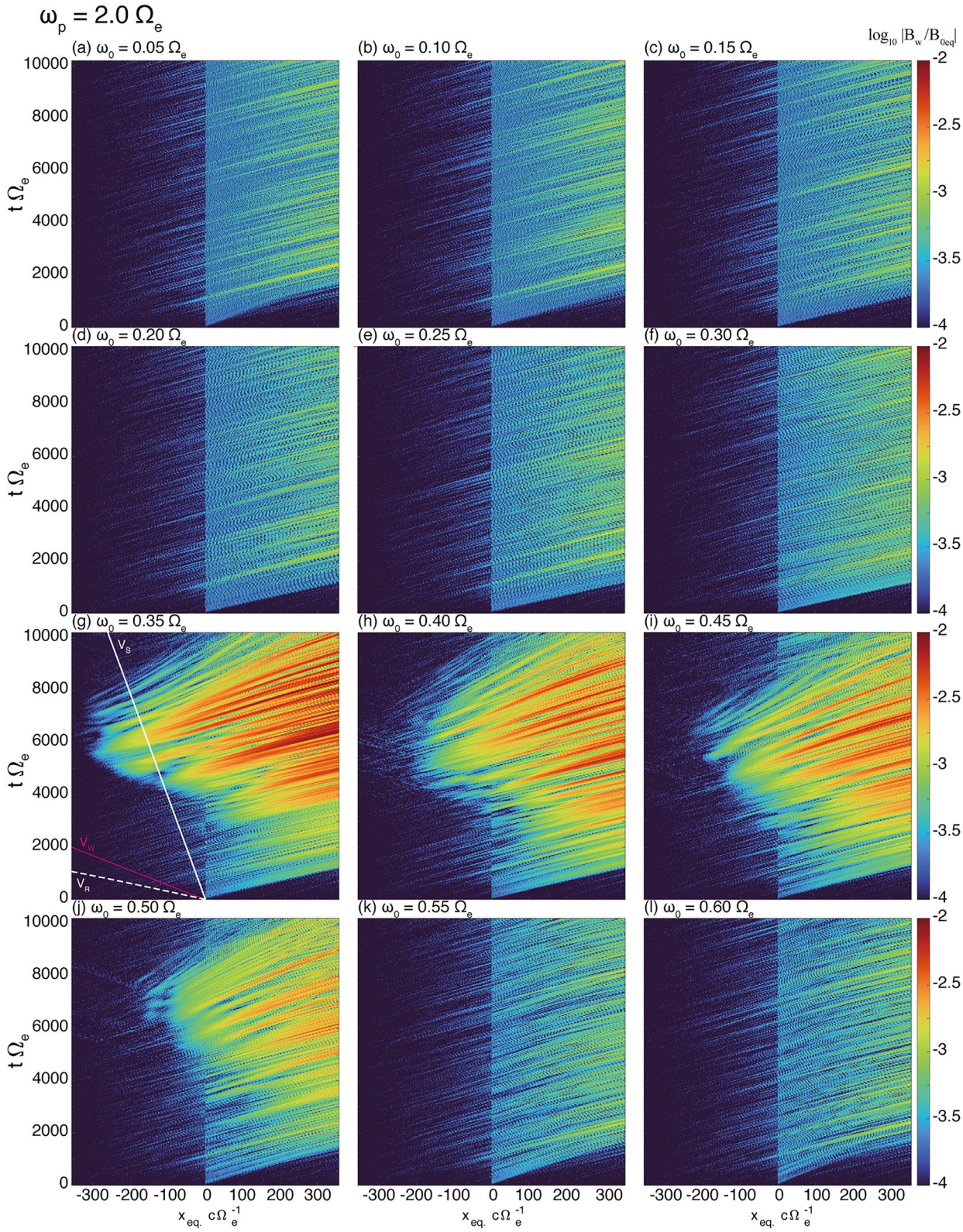

Figure 7. Spatial and temporal profiles of magnetic fields for forward waves for Case 3 with plasma frequency $\omega_p = 2.0\Omega_e$ and triggering wave frequencies ω_0 from (a) $0.05\Omega_e$ to (l) $0.60\Omega_e$, respectively. (g) (solid magenta line) The velocity of wave generation V_W, (dashed white line) the resonance velocity for 100 keV electrons at the magnetic equator, (solid white line) the source velocity V_S for 100 keV electrons at the magnetic equator.

of the subpackets smoothly moves upstream. Figures 8a–8l show spatial and temporal profiles of instantaneous frequencies for forward propagating triggered emissions for the plasma frequency $\omega_p = 2.0\Omega_e$. We find that triggered emissions in Figures 8g–8j are rising-tone emissions. The instantaneous frequencies of these cases smoothly increase from the frequencies of triggering waves.

Rising-tone emissions are observed in all three cases described above. The generation regions of rising-tone emissions shift upstream from the triggering waves. We have shown that the source velocity varies depending on the triggering wave frequency and the energy of resonant electrons. The source velocity dynamically changes in the formation process of the rising-tone emissions with increasing frequencies. Comparing wave generation velocities for upstream shifts of the triggered emissions in Figures 4, 6, and 8 with the source velocity (V_S) in Figure 2, we confirm the variation of the source velocity by changing the frequency of the triggering waves. The duration of the subpacket structure depends on the plasma frequency and the frequency of triggering waves. We discuss the formation process of rising-tone emissions based on the source velocity and subpacket structures in the following sections.

3.1. Triggering Wave Frequencies

Parametric surveys on plasma frequency and triggering wave frequency have shown that rising-tone triggered emissions are observed over a certain frequency range of triggering waves. This section discusses how the triggering wave frequency controls the generation of triggered emissions. Nonlinear wave growth takes place when the amplitude of the triggering wave is greater than the threshold amplitude $\Omega_{\rm op}$, and less than the optimum amplitude $\Omega_{\rm th}$. Figure 1a indicates that the minimum frequency satisfying the condition is $0.35\Omega_e$, $0.15\Omega_e$, and $0.12\Omega_e$ for the plasma frequencies $\omega_p = 2.0\Omega_e$, $4.0\Omega_e$, and $6.0\Omega_e$, respectively. We find triggered emissions with triggering waves at frequencies from $0.35\Omega_e$, $0.20\Omega_e$, and $0.15\Omega_e$ for plasma frequencies $\omega_p = 2.0\Omega_e$, $4.0\Omega_e$, and $6.0\Omega_e$ as shown in Figures 3, 5 and 7, respectively. The results are consistent in terms of the prerequisite of the nonlinear theory given by optimum and threshold amplitudes, supporting that nonlinear wave growth is a dominant process in the generation of rising-tone triggered emissions.

The maximum frequency of the triggering wave for generating triggered emissions are $\omega = 0.5\Omega_e$, $0.3\Omega_e$, and $0.2\Omega_e$ for the plasma frequency $\omega_p = 2.0\Omega_e$, $4.0\Omega_e$, and $6.0\Omega_e$ in Figures 5d, 3f, and 7j. In frequency ranges higher than these threshold frequencies for triggered emissions, the conditions for optimum and threshold amplitude are satisfied. There is another condition that controls the generation of triggered emissions. Nonlinear wave growth involves two phases, which are absolute instability and convective wave growth. Absolute instability is defined as wave growth in time at a fixed position ($\partial\Omega_w/\partial t > 0$), which is dominant in the early phase of triggered emissions. Convective wave growth is the amplitude increase of a seed wave generated from the absolute instability in a frame of reference moving with the group velocity. Since we find no emission in the higher frequency range, the absolute instability is suppressed because the generation region for triggered emissions does not distribute over the upstream region of triggering waves. The motion of generation region is given by the source velocity V_S plotted in Figure 2. The source velocity is less than $-0.1c$ in magnitude or positive values for 10–100 keV electrons. With a small magnitude or a positive value of the source velocity, the generation region of triggered emissions does not expand over the interaction region. Assuming the constant growth rate in the vicinity of the equator, we can derive that the upstream shift of the generation region is required for obtaining the absolute instability growing from the same level of thermal fluctuations of the wave fields over the frequency range of emissions. We discuss the upstream shift of the generation region and the generation process in Section 3.2. For obtaining continuous subpacket emissions with long duration, both nonlinear wave growth conditions $\Omega_{\rm op} > \Omega_{\rm th}$ and the upstream expansion of the generation region are required. The distribution and expansion of the generation region are strongly related to the generation process of triggered emissions.

3.2. Upstream Shift of Generation Region

With the plasma frequency $4.0\Omega_e$, we observe the generation of strong long wave packets forming rising-tone emissions in Figures 3d–3f, where the generation region of the subpackets moves to the upstream region of the triggering wave. In Figure 3d, the velocity of the upstream shift of the wave generation region (V_w) for forward propagating waves at the equator is approximately $-0.12c$, indicated by a solid magenta line. The velocity is smaller than the resonance velocity $V_R = -0.35c$ in magnitude with $\omega = 0.2\Omega_e$ at the equator shown in white

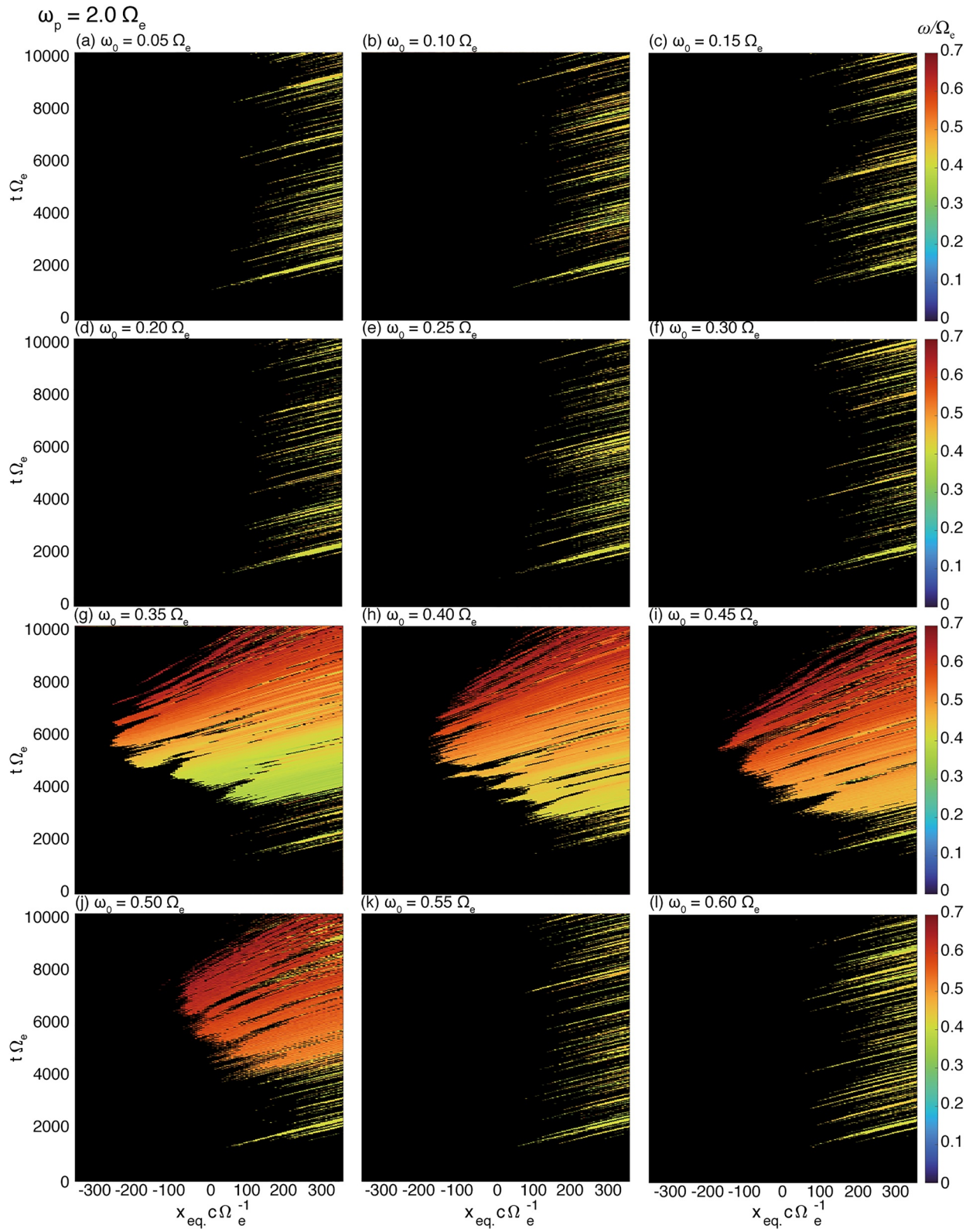

Figure 8. Spatial and temporal profiles of instantaneous frequency of triggered emissions for Case 3 with the plasma frequency $\omega_p = 2.0\Omega_e$ and different triggering wave frequencies ω_0 from (a) $0.05\Omega_e$ to (l) $0.60\Omega_e$, respectively.

dashed line for 100 keV resonant electrons. Because the formation of the resonant current causes the generation of rising-tone emissions moving with the group velocity, the spatial structure of the resonant current moves at a different speed from the resonance velocity. Nogi and Omura (2022) have introduced the concept of the source velocity, which describes the velocity of the spatial structure of resonant current, given by $V_S = V_R + V_g$. We find the velocity of the upstream shift of the wave generation region is in good agreement with the source velocity for 100 keV electrons.

The source velocity V_S is plotted as a function of frequency for different kinetic energies 10, 50, 100, and 200 keV for $\omega_p = 4.0\Omega_e$ in Figure 2b. As the frequency of the triggering wave increases from $0.2\Omega_e$, the magnitude of the source velocity decreases, while the resonance energy decreases and compensates for the decreasing source velocity. Thus, the generation region shifts upstream with nearly a constant velocity. The condition of the absolute instability gives a necessary condition of $V_S < 0$ for triggering new emissions.

Throughout the generation of rising-tone emissions, the triggered subpacket continuously modulates the phase space distribution of counter-streaming resonant electrons, and the phase-modulated electrons form a subsequent subpacket. The process takes place repeatedly during the generation of triggered emissions. We have confirmed that the upstream motion of the generation region for the plasma frequency $4.0\Omega_e$ agrees with the source velocity. When the source velocity becomes positive in the generation process of a series of subpackets at progressively higher frequencies, the generation process comes to an end with the formation of small subpackets, as we find in Figures 3d–3f.

In the cases of $\omega_p = 6.0\Omega_e$ and $\omega_p = 2.0\Omega_e$, we find that the generation region of subpacket moves with different velocities from the source velocity. Figure 5c indicates that the velocity of the generation region shown in the solid magenta line is smaller in magnitude than the source velocity shown in the solid white line. Figure 7g shows an opposite tendency that the velocity of the generation region shown in the solid red line is greater than the source velocity shown in the solid white line. We also find that the duration and intensity of the subpacket in those cases are different from the case of $\omega_p = 4.0\Omega_e$. Comparing Figure 3d with Figures 5c and 7g, we find that the durations of the subpackets are different. In the next section, we discuss the discrepancy in the velocity of the wave generation region by comparing the formation processes of subpackets in the three cases.

3.3. Subpacket Formation and Motion of Generation Regions

The concept of the source velocity is based on the formation of the resonant current caused by the phase-organized electrons. The formation of subpacket structures of rising-tone emission gives rise to deviation of the wave generation point from the source velocity. We extend the concept of the source velocity V_S to include the motion of the generation point of subpackets, and define the velocity of the wave generation point as V_W given by

$$V_W = pV_R + qV_g, \quad \text{where} \begin{cases} p = 1 \quad \text{and} \quad q = 1, & \text{or} \\ 0 < p < 1 \quad \text{and} \quad q = 1, & \text{or} \\ p = 1 \quad \text{and} \quad 0 < q < 1. \end{cases} \tag{6}$$

When the continuous formation of a wave packet takes place as shown in Case 1 ($\omega_p = 4.0\Omega_e$), the velocity of wave generation V_W is identical to the source velocity, which corresponds to $p = q = 1$ in Equation 6. When the formation of a wave packet is interrupted because of the damping phase of the wave packet after the saturation, as shown in Case 3 ($\omega_p = 2.0\Omega_e$), there arises a gap between the first wave packet and the subsequent wave packet. The results in the absence of wave propagation over the gap, which can be represented by the reduced factor q ($0 < q < 1$) of V_g and $p = 1$. As shown in Case 2 ($\omega_p = 6.0\Omega_e$), the formation of the resonant current is delayed, and the period of the nonlinear wave growth is shortened. The reduction of the nonlinear wave growth period can be represented by the reduced factor p ($0 < p < 1$) of V_R and $q = 1$. The schematic illustrations of the generation process of subpacket structure are shown in Figure 9.

Figure 10 shows spatial distribution of frequency spectra. In Figure 10a, three subpackets are formed with discrete frequency gaps, and the instantaneous frequency of each subpacket continuously increases as shown by arrows for sp_1, sp_2, and sp_3. Between sp_2 and sp_3, the subpackets are overlapped at $x = 200c\Omega_e^{-1}$. The frequency of the beginning of the latter subpacket shown as sp_3 is less than or equal to the frequency at the termination of the former

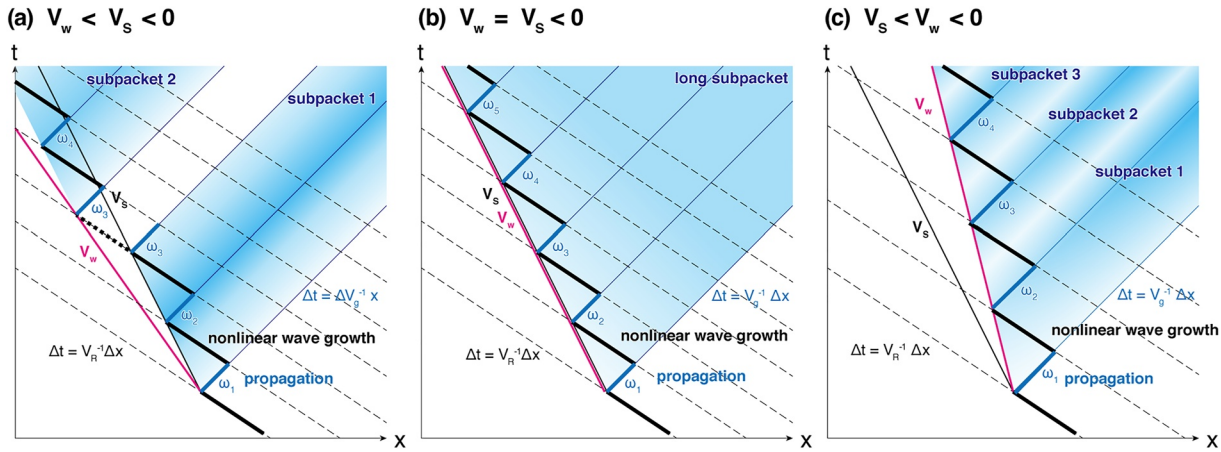

Figure 9. Schematic illustrations of the generation processes of subpacket structure with different velocities of wave generation; (a) The velocity of wave generation V_W is less than the source velocity $V_S = V_R + V_g$. (b) V_W is equal to V_S. (c) V_W is greater than V_S.

subpacket as sp_2. The frequency discontinuity between subpackets remains in the later phase of triggered emissions, as shown in Figure 10b. Because the group velocity with the frequency greater than $0.25\Omega_e$ monotonically decreases as the frequency increases, the separation distance between sp_2 and sp_3 increases through propagation.

Figure 9a shows a schematic illustration of the generation process of short subpackets in Case 3. The dashed blue lines indicate trajectories of resonance electrons moving at the resonance velocity, and the solid blue lines indicate the propagation of triggered waves with the group velocity. The solid thin black line indicates the source velocity V_S, and the magenta line indicates the velocity of the wave packet V_W. The first subpacket is triggered from the injected triggering waves, and the generation of waves continuously takes place along V_S in a subpacket, forming a greater resonant current from ω_1 to ω_2. Wave amplitude of the triggered subpacket approaches to the optimum amplitude by virtue of greater resonant current, and the nonlinear wave growth is suppressed in the later phase of the subpacket from ω_2 to ω_3. The phase organization of resonant electrons is enhanced in the vicinity of the propagation path of the wave packet with ω_2. In contrast, the release of the phase structure is suppressed due to the weak amplitude in the termination of the first subpacket, as shown in the bold black line toward ω_3. The phase-organized electrons keep their spatial structure with phase space modulation, and some of the phase-organized electrons are carried with the resonance velocity as shown in the dashed black line, and the second subpacket is generated. As a result, the velocity of the generation point over the multiple subpackets (V_W) becomes less than V_S. This generation model of the short subpacket is similar to that by Hanzelka et al. (2020), while our new model indicates that the motion of each subpacket is given by the source velocity.

When a triggered wave packet is long enough in space and time, the generation region moves with the source velocity as we find in Case 1 ($\omega_p = 4.0\Omega_e$) shown in Figures 3 and 4. With the plasma frequency $4.0\Omega_e$ and triggering wave frequency $0.25\Omega_e$, we observe the formation of multiple subpackets, while the spectrum analyses indicate that a single long sustaining subpacket is generated in the vicinity of the generation region as shown in Figures 10c, 11b3, and 11b4. Figure 9b shows a schematic illustration of the generation process of a triggered emission for a long subpacket. In the long-sustaining subpacket, phase-organized particles by the triggered wave generate a subsequent wave with a slightly higher frequency, and the subsequent wave modulates fresh resonant electrons. These microscopic processes continuously take place in the vicinity of the generation region, which moves upstream from the triggering wave. For a long subpacket generation, the velocity of the wave packet (V_W) and the source velocity are approximately the same negative value so that the absolute instability is maintained in the generation region. When the magnitude of the source velocity is small, the growth rate of the absolute instability at a fixed position becomes small.

When the triggering wave is injected with a frequency $0.15\Omega_e$ in Case 2 ($\omega_p = 6.0\Omega_e$), two long subpackets separated at $0.25\Omega_e$ are generated in the vicinity of the generation region in Figure 11c3. The wave growth and frequency sweep rate below $0.25\Omega_e$ is weaker than those above $0.25\Omega_e$. The subpacket splits into multiple short subpackets through convective wave growth. Nonlinear wave growth in the upstream region of the equator is weaker than in other cases with $\omega_p = 2.0\Omega_e$ and $4.0\Omega_e$. Figure 9c shows the schematic illustration of the generation process with $\omega_p = 6.0\Omega_e$. The ratio of the duration of the nonlinear wave growth to the propagation time of triggered waves becomes small, and the source velocity becomes small, while its value is still negative.

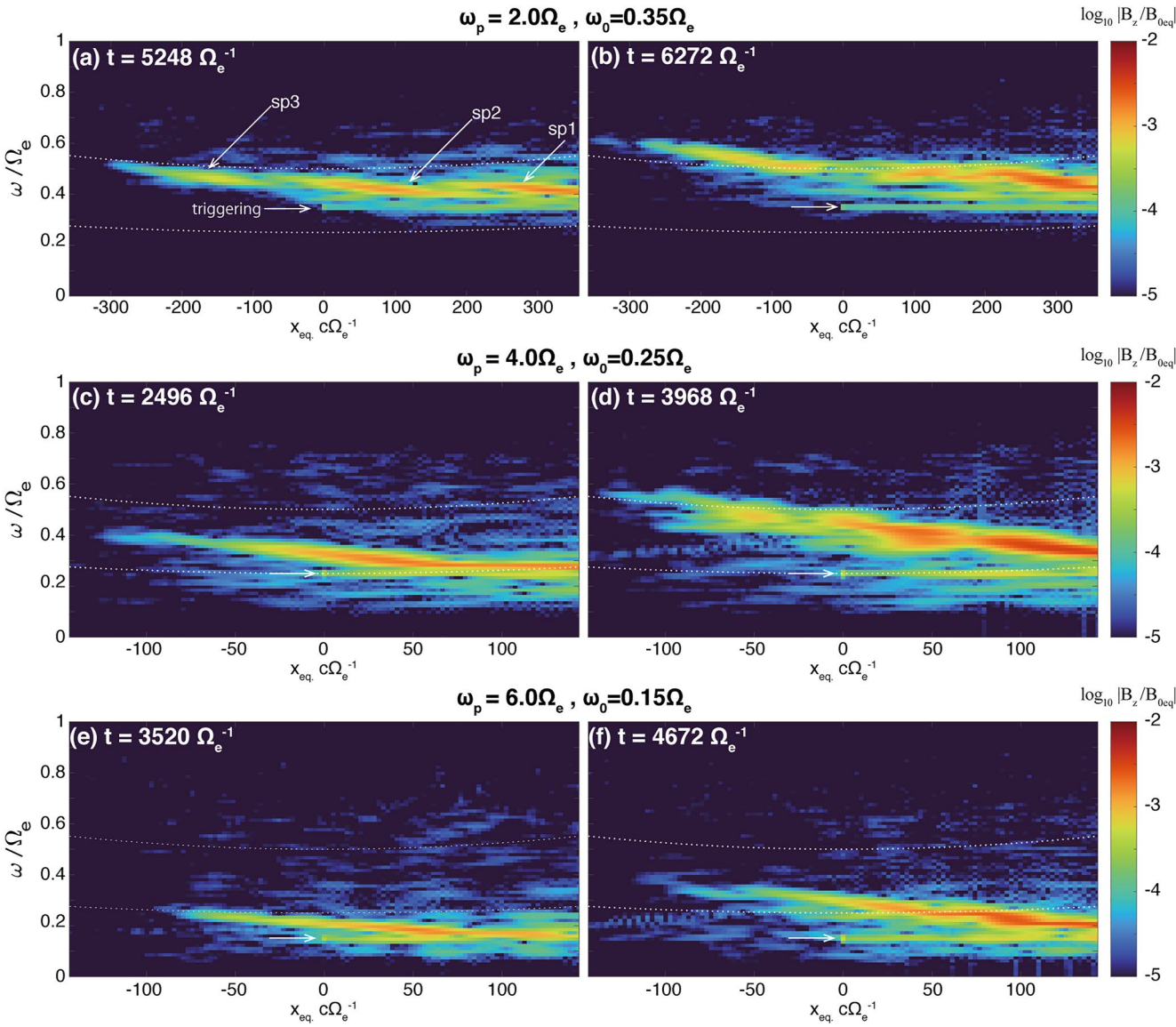

Figure 10. Snapshots of the spatial distribution of wave frequencies for plasma frequencies, (a, b)$\omega_p = 2.0\Omega_e$, (c, d) $4.0\Omega_e$ and (e, f) $6.0\Omega_e$, respectively; (dotted lines) One quarter and one half of the local electron cyclotron frequencies. (white arrows) the injection point and frequency of triggering wave.

The wave packets below the frequency $0.25\Omega_e$ are grouped together because of the variation of group velocity $\partial V_g/\partial\omega > 0$. As we find in Figure 2, the group velocity increases with the increasing frequency and maximizes at $\omega = 0.25\Omega_e$. When a rising-tone emission is started below $0.25\Omega_e$, a lower frequency packet is generated first, followed by a higher frequency packet with a higher group velocity. The higher frequency wave packet has a tendency to catch up with the lower frequency wave packet. Because of this dispersion effect, the subpackets with frequencies below $0.25\Omega_e$ have a tendency to coalesce with each other, as we find in Figure 5c. In the corresponding spatial and temporal profile of the magnetic field, we observe that several subpackets cross at a certain point, as shown by the arrow in Figure 11c5. The coalescence of wave packets below $0.25\Omega_e$ is in agreement with the observation results reported by Foster et al. (2017).

When the electron holes are formed with two different frequency waves, while the trajectories of trapped and untrapped particles with two waves are mutually independent, we can regard each wave as coherent in terms of nonlinear wave-particle interaction (Omura, 2021). When a long triggered wave is generated as in Case 1 ($\omega_p = 4.0\Omega_e$), the criterion of coherence is satisfied in both the upstream region and the downstream region of the triggering waves. In Case 2 ($\omega_p = 6.0\Omega_e$), on the other hand, the new wave packets overtake the waves with lower

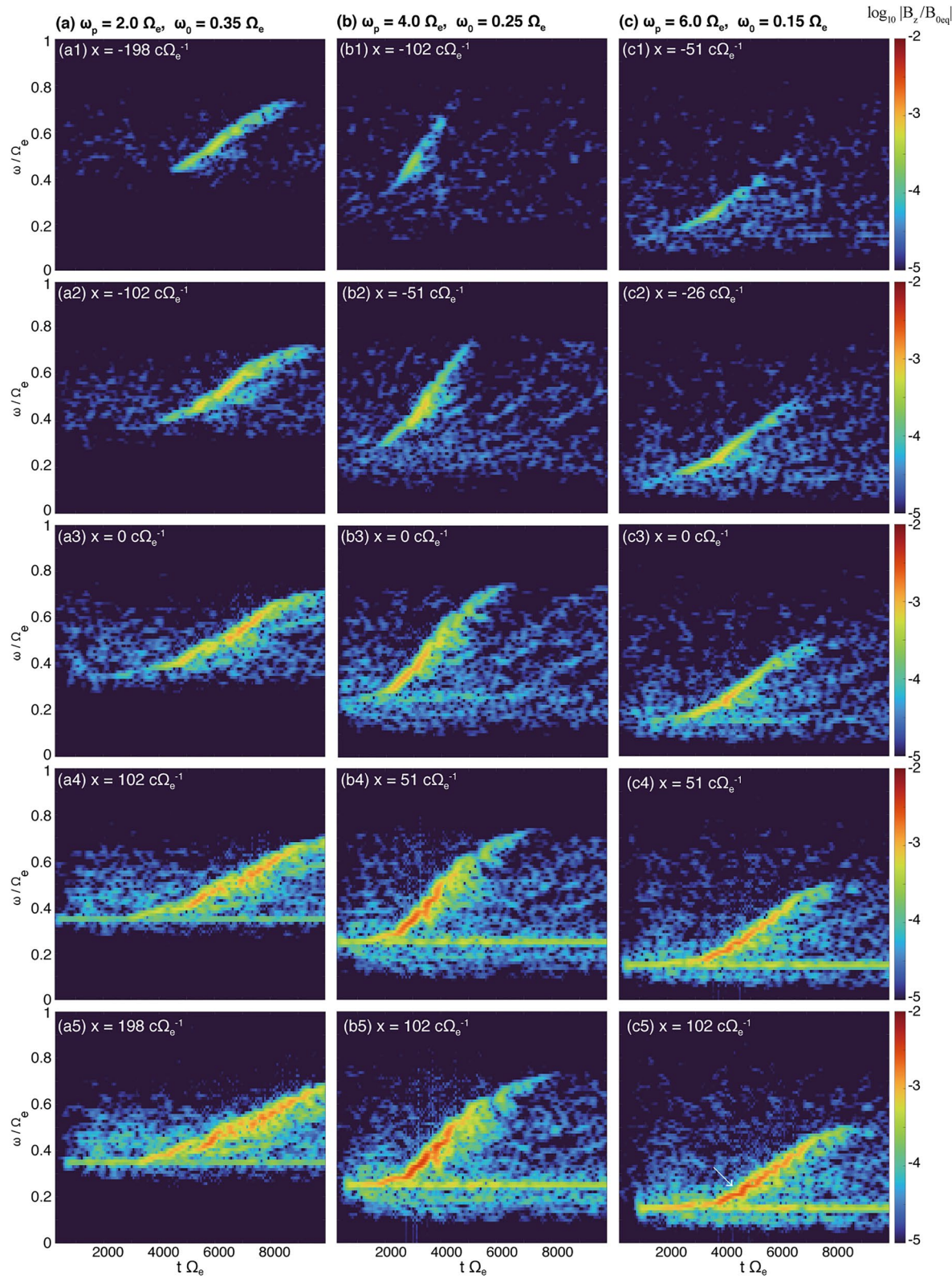

Figure 11. Dynamic spectra of distinct rising-tone emissions for plasma frequencies (a) $\omega_p = 2.0\Omega_e$, (b) $\omega_p = 4.0\Omega_e$, and (c) $\omega_p = 6.0\Omega_e$ at different positions indicated by labels (a1−a5), (b1−b5), and (c1−c5), respectively, which correspond to positions from the upstream region to the downstream region for forward propagating waves.

frequencies in the upstream region of triggering waves, and the coherence of the waves in the generation region deteriorates. The formation of resonant currents becomes less effective, and the generation of wave packets is interrupted, resulting in the generation of a short subpacket in Case 2.

3.4. Dynamic Frequency Spectra

Figure 11 shows dynamic spectra observed at different positions for forward propagating waves from upstream to downstream for different plasma frequencies, (a) $2.0\Omega_e$, (b) $4.0\Omega_e$, and (c) $6.0\Omega_e$. We plot the dynamic spectra for the runs with the frequencies of triggering wave (a) $0.35\Omega_e$, (b) $0.25\Omega_e$, and (c) $0.15\Omega_e$, in which triggered emissions are observed. From the top to the bottom of each column, we plot dynamic spectra observed at different positions from the upstream region to the downstream region for forward propagating waves. We perform short-time discrete Fourier transformation for forward propagating waves with a window size $\Delta t = 512\Omega_e^{-1}$, which has 65,536 data points and shifting the window by $64\Omega_e^{-1}$, corresponding to 8,192 data points. In all cases shown in Figure 11, we find that triggered emissions show rising-tone frequencies. The frequency of the triggered waves increases monotonically in the generation region in Figures 11b1 and 11c1, while the frequency increase is suppressed between the subpackets in Figure 11a1.

In the case with $\omega_p = 2.0\Omega_e$ and $\omega_0 = 0.35\Omega_e$, relatively short subpackets are generated throughout the emission as shown in Figures 11a1–11a5. The generation region moves from the downstream region to the upstream region of the magnetic equator, and the frequency gap between subpackets enlarges as the triggered waves propagate, resulting in the discontinuity of the frequency variations between subpackets as shown in Figures 11a3 and 11a4. The generation of short subpackets and the frequency gap between subpackets are consistent with the generation model of the subpackets illustrated in Figure 9a.

Continuous long subpackets are observed in the generation region of the upstream region of triggered emissions with $\omega_p = 4.0\Omega_e$ and $\omega_0 = 0.35\Omega_e$ as shown in Figures 11b1 and 11b2. The instantaneous frequencies of triggered emissions are greater than $0.25\Omega_e$, and continuous formation of the resonant current takes place as illustrated in Figure 9b.

In the case with $\omega_p = 6.0\Omega_e$ and $\omega_0 = 0.15\Omega_e$, the weak long subpacket is generated in the upstream region as shown in Figure 11c1. The generation region of the subpackets with the frequency below $0.25\Omega_e$ exists in the vicinity of the equator in Figures 11c2 and 11c3. Figures 11c2 and 11c3 clearly show the frequency sweep rate below $0.25\Omega_e$ is smaller than those above $0.25\Omega_e$. We observe that the wave amplitude is enhanced at $0.25\Omega_e$ as indicated by a white arrow in Figure 11c5. Because the magnitude of group velocity maximizes at $0.25\Omega_e$, the wave packets converge in the downstream region of triggered emissions as discussed above.

Falling-tone emissions are generated from rising-tone triggered emissions in the higher frequency range in Figures 11a4, 11a5, 11b4, 11b5, and 11c5. Falling-tone emissions are triggered by the termination of short rising-tone emissions in the downstream region of the subpackets. Ground observation of VLF triggered emissions have shown that shorter wave duration of injected waves leads to the generation of falling-tone emissions (Helliwell & Katsufrakis, 1974). Nogi et al. (2020) have reproduced falling-tone emissions by using similar parameters to the present paper, and the difference from the present paper is the duration period of triggering waves. Short-period triggering waves around half the cyclotron frequency lead to falling-tone emissions, and long-period triggering waves lead to rising-tone emissions. The generation of falling-tone emissions from a short rising-tone subpacket supports that the enhancement of trapping of resonant electrons forming electron hills is caused by short triggering waves. In the case with $\omega_p = 2.0\Omega_e$, falling-tone emissions are generated from rising-tone emissions with the frequency range from $0.5\Omega_e$ to $0.7\Omega_e$, which is upper-band chorus emissions. Liu et al. (2021) have shown by using Van Allen Probes that the initial frequency of distinct falling-tone subpackets gradually increases, and the sequence of the initial part of subpackets is aligned as upper-band rising-tone emissions. The present result shown in Figure 11a5 is similar to the observation result by Liu et al. (2021), except for the frequency gap between lower-band and upper-band chorus emissions. Because the parallel propagation in the one-dimensional model is assumed in the present simulation, the frequency gap due to nonlinear damping through Landau resonance cannot be formed.

3.5. Evolution of Velocity Distribution Function

Figure 12 shows the velocity distribution of energetic electrons in the vicinity of the magnetic equator. The initial velocity distribution function f_0 is shown in Figures 12a and 12b for Case 3 ($\omega_p = 2.0\Omega_e$) and Case 2 ($\omega_p = 6.0\Omega_e$), respectively. Figures 12c–12h show the differences from the initial velocity distribution function for

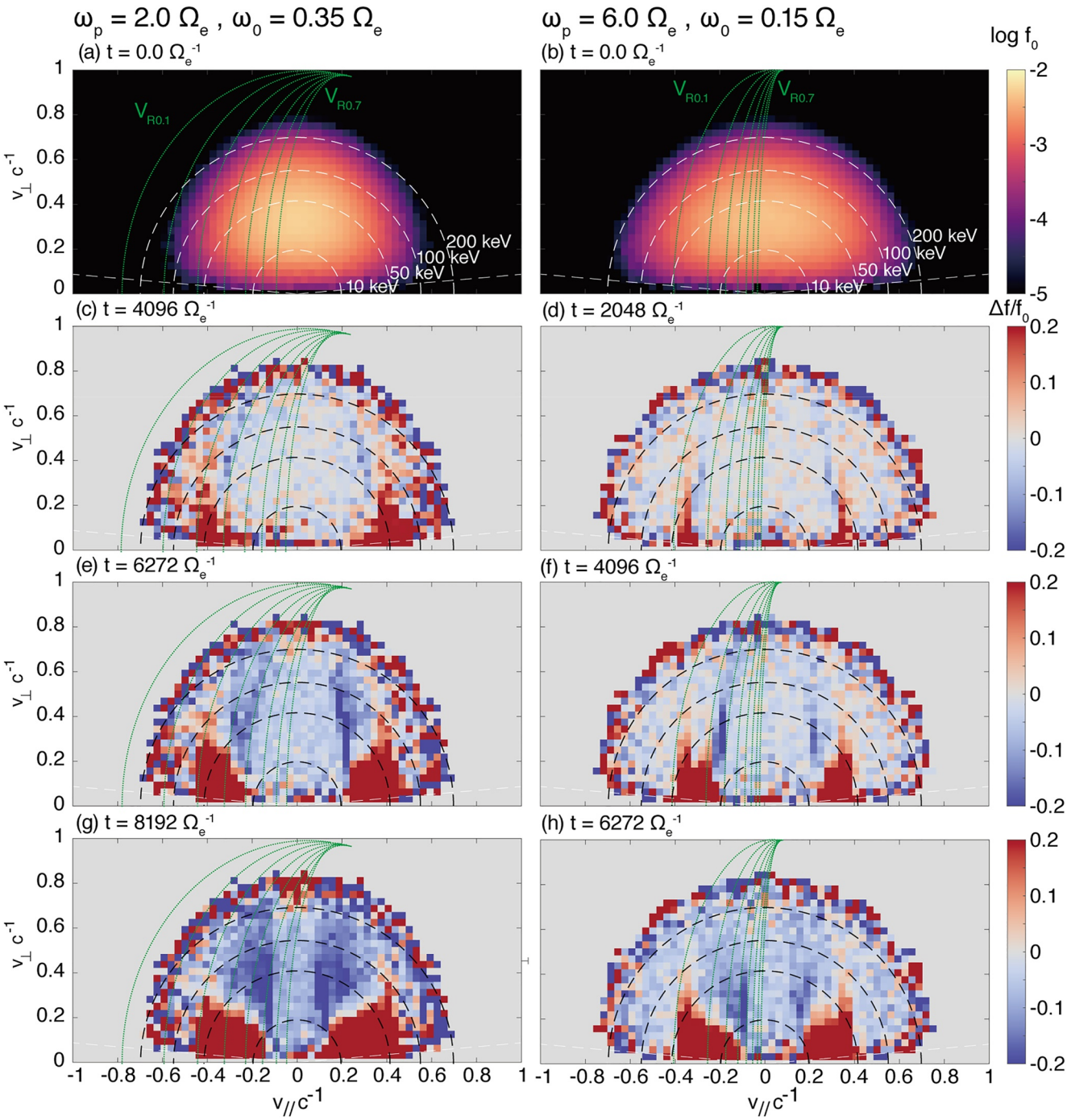

Figure 12. Time evolution of velocity distributions of energetic electrons at the equator for plasma frequencies, $\omega_p = 2.0\Omega_e$ and $6.0\Omega_e$ with triggering wave frequencies $\omega_0 = 0.35\Omega_e$ and $0.15\Omega_e$, respectively; (a, b) The initial distribution f_0, (c, d) f/f_0 variation from the initial distribution at the beginning, (e, f) the middle, and (g, h) the end of triggered emissions. Green lines show resonance velocities for frequencies from $0.1\Omega_e$ to $0.7\Omega_e$.

(c, d) beginning of the triggered emissions, (e, f) middle phase of the triggered emissions, and (g, h) termination of the triggered emissions, respectively. The variation of the velocity distribution for $\omega_p = 4.0\Omega_e$ with triggering wave $0.3\Omega_e$ is presented in figure 11 of Nogi and Omura (2022).

The density modulation in velocity phase space takes place in the vicinity of the resonance velocity, shown with green lines in Figures 12a–12h. In the case with the plasma frequency $2.0\Omega_e$, we find that the resonance velocity varies from the frequency for $0.40\Omega_e$, $0.45\Omega_e$, and $0.65\Omega_e$ in Figures 12c–12g, respectively. The frequencies

for the resonance velocities at which the depletion of phase space density is formed are in agreement with the instantaneous frequency at the equator, as shown in Figure 11a3. With $\omega_p = 6.0\Omega_e$, we have confirmed that the frequencies for resonance velocities of the density depletion are consistent with the instantaneous frequency in Figure 11c3.

The energy range for the case with $\omega_p = 2.0\Omega_e$ is presumed to be from 50 to 100 keV in the initial phase, 10–50 keV in the end of triggered emissions. The effective energy range of nonlinear growth of chorus emissions is 10−100 keV. In this energy range, we find a relatively strong depletion of electrons in Figure 12. Resonant electrons forming a hole in velocity phase space are scattered to lower pitch angles, and some of them get into the loss cone. In the energy range of 10−40 keV, we can find strong precipitation due to the generation of chorus emissions. The acceleration of electrons takes place in the higher energy range as we find an enhanced electron flux around 90° of pitch angle in Figure 12g.

Comparing Figure 12c with Figure 12d, we find the difference in the depth of the electron hole. In the case with $\omega_p = 2.0\Omega_e$, intense modulation of the density takes place due to a deeper electron hole (= greater Q value), leading to greater resonant current than that with $\omega_p = 6.0\Omega_e$. The initial difference in the intensity of the resonant current controls the absolute and convective growth rates, and frequency sweep rate. In the case with $\omega_p = 6.0\Omega_e$, the modulation of the phase space density due to formation of the electron hole is suppressed at the initial phase of the triggered emissions, as shown in Figure 12d. The forgoing subpacket at $0.20\Omega_e$ is overtaken by the subsequent subpacket at $0.25\Omega_e$, and coherent nonlinear wave-particle interaction is suppressed.

4. Summary and Discussion

We have performed simulations of whistler-mode wave-particle interaction in a parabolic magnetic field with 12 different frequencies of triggering waves and 3 different plasma frequencies specifying cold plasma densities. Under a given plasma condition, specific frequency ranges of the triggering wave generate rising-tone emissions. We summarise the characteristics of triggered emissions as follows.

1. The generation regions of rising-tone emissions move upstream from the triggering waves.
2. The source velocity represents the motion of resonant current, while the velocity of the wave generation includes formation processes of subpackets and their intervals. The velocity of wave packet generation is dependent on the duration of the subpacket controlled by the formation time of resonant current in the generation region.
3. When the source velocity is approximately the same as the velocity of wave packet generation, resonant current is formed continuously, leading to a long-sustaining rising-tone emission.
4. When the spatial and temporal gap between subpackets exists due to the damping phase of the generation of a short subpacket, resonant electrons in the gap of the subpacket are carried at the resonance velocity to the upstream region, forming subsequent subpacket. As a result, the velocity of wave generation increases in magnitude.
5. When the formation of resonant currents is delayed, the velocity of wave generation becomes smaller than the source velocity in magnitude. Coalescence of subpackets takes place below the frequency $0.25\Omega_e$, delaying formation of the resonant current in the generation region.
6. As a condition for an absolute instability of the wave, the source velocity should be a small negative value. Namely, a gradual upstream shift of the source region is necessary for the wave to grow locally.
7. In the frequency range for the upper-band chorus of rising-tone emissions, short falling-tone packets are generated along with rising-tone packets.

In the present study, we have observed the generation of rising-tone emissions from the triggering waves below one half of the cyclotron frequency. The maximum frequency of rising-tone triggered emissions is greater than half the cyclotron frequency, while we have not observed frequency gap at $0.5\Omega_e$, which is typically observed in chorus waves. Ratcliffe and Watt (2017) have proposed the model that modulated electron distribution function is formed and two distinct peaks of linear growth rate in frequency appear, resulting in the generation of lower-band and upper-band chorus emissions. The modulation in the velocity distribution function in frequency can be caused by Landau resonance (Li et al., 2019, 2022; Sauer et al., 2020).

We have assumed parallel propagation of whistler-mode waves by taking the one-dimensional simulation system along the magnetic field line. Since there arises no electric field in the parallel direction, we have neglected the

electrostatic field. The rising-tone emissions crossing half the cyclotron frequency are expected to undergo damping near the local cyclotron frequency, resulting in lower-band and upper-band emissions (Hsieh & Omura, 2018; Omura et al., 2009). Self-consistent simulations in a two-dimensional system are necessary for confirmation of the gap formation in the rising-tone emissions propagating obliquely to the magnetic field. Such a two-dimensional simulation was performed by Ke et al. (2017). They did not find the gap formation possibly because of the smallness of the simulation system. Two-dimensional simulations with sufficiently large spatial extent are left as a future study.

Data Availability Statement

The simulation data are open to the public on the web (https://doi.org/10.5281/zenodo.7022941). The simulation data used in this paper are obtained from KEMPO1 code (http://space.rish.kyoto-u.ac.jp/software/) with minor modifications by Nogi et al. (2020).

Acknowledgments
The computer simulation in the present study was performed on the KDK computer system at Research Institute for Sustainable Humanosphere, Kyoto University. This work was supported by JSPS KAKENHI Grants JP17H06140 and JP20H01960.

References

Chen, H., Gao, X., Lu, Q., Fan, K., Ke, Y., Wang, X., & Wang, S. (2022). Gap formation around $0.5\Omega_e$ in the whistler-mode waves due to the plateau-like shape in the parallel electron distribution: 2D pic simulations. *Journal of Geophysical Research: Space Physics*, *127*(5), e2021JA030119. https://doi.org/10.1029/2021JA030119

Chen, H., Gao, X., Lu, Q., Sauer, K., Chen, R., Yao, J., & Wang, S. (2021). Gap formation around $0.5\Omega_e$ of whistler-mode waves excited by electron temperature anisotropy. *Journal of Geophysical Research: Space Physics*, *126*(2), e2020JA028631. https://doi.org/10.1029/2020JA028631

Foster, J. C., Erickson, P. J., & Omura, Y. (2021). Subpacket structure in strong VLF chorus rising tones: Characteristics and consequences for relativistic electron acceleration. *Earth Planets and Space*, *73*(1), 140. https://doi.org/10.1186/s40623-021-01467-4

Foster, J. C., Erickson, P. J., Omura, Y., Baker, D. N., Kletzing, C. A., & Claudepierre, S. G. (2017). Van allen probes observations of prompt MeV radiation belt electron acceleration in nonlinear interactions with VLF chorus. *Journal of Geophysical Research: Space Physics*, *122*(1), 324–339. https://doi.org/10.1002/2016JA023429

Fujiwara, Y., Nogi, T., & Omura, Y. (2022). Nonlinear triggering process of whistler-mode emissions in a homogeneous magnetic field. *Earth Planets and Space*, *74*(1), 95. https://doi.org/10.1186/s40623-022-01646-x

Gołkowski, M., Harid, V., & Hosseini, P. (2019). Review of controlled excitation of non-linear wave-particle interactions in the magnetosphere. *Frontiers in Astronomy and Space Sciences*, *6*, 2. https://doi.org/10.3389/fspas.2019.00002

Hanzelka, M., Santolík, O., Omura, Y., Kolmašová, I., & Kletzing, C. A. (2020). A model of the subpacket structure of rising tone chorus emissions. *Journal of Geophysical Research: Space Physics*, *125*(8), e2020JA028094. https://doi.org/10.1029/2020JA028094

Harid, V., Gołkowski, M., Hosseini, P., & Kim, H. (2022). Backward-propagating source as a component of rising tone whistler-mode chorus generation. *Frontiers in Astronomy and Space Sciences*, *9*, 232. https://doi.org/10.3389/FSPAS.2022.981949

Helliwell, R. A. (1967). A theory of discrete VLF emissions from the magnetosphere. *Journal of Geophysical Research*, *72*(19), 4773–4790. https://doi.org/10.1029/JZ072i019p04773

Helliwell, R. A., & Katsufrakis, J. P. (1974). VLF wave injection into the magnetosphere from siple station, Antarctica. *Journal of Geophysical Research*, *79*(16), 2511–2518. https://doi.org/10.1029/JA079i016p02511

Hikishima, M., & Omura, Y. (2012). Particle simulations of whistler-mode rising-tone emissions triggered by waves with different amplitudes. *Journal of Geophysical Research: Space Physics*, *117*(A4), A04226. https://doi.org/10.1029/2011JA017428

Hikishima, M., Omura, Y., & Summers, D. (2010). Self-consistent particle simulation of whistler mode triggered emissions. *Journal of Geophysical Research: Space Physics*, *115*(A12), A12246. https://doi.org/10.1029/2010JA015860

Hikishima, M., Yagitani, S., Omura, Y., & Nagano, I. (2009). Full particle simulation of whistler-mode rising chorus emissions in the magnetosphere. *Journal of Geophysical Research: Space Physics*, *114*(A1), A01203. https://doi.org/10.1029/2008JA013625

Hsieh, Y.-K., & Omura, Y. (2018). Nonlinear damping of oblique whistler mode waves via Landau resonance. *Journal of Geophysical Research: Space Physics*, *123*(9), 7462–7472. https://doi.org/10.1029/2018JA025848

Juhász, L., Omura, Y., Lichtenberger, J., & Friedel, R. H. (2019). Evaluation of plasma properties from chorus waves observed at the generation region. *Journal of Geophysical Research: Space Physics*, *124*(6), 4125–4136. https://doi.org/10.1029/2018JA026337

Katoh, Y., & Omura, Y. (2006). A study of generation mechanism of VLF triggered emission by self-consistent particle code. *Journal of Geophysical Research: Space Physics*, *111*(A12), A12207. https://doi.org/10.1029/2006JA011704

Ke, Y., Gao, X., Lu, Q., Wang, X., & Wang, S. (2017). Generation of rising-tone chorus in a two-dimensional mirror field by using the general curvilinear pic code. *Journal of Geophysical Research: Space Physics*, *122*(8), 8154–8165. https://doi.org/10.1002/2017JA024178

Kubota, Y., Omura, Y., Kletzing, C., & Reeves, G. (2018). Generation process of large-amplitude upper-band chorus emissions observed by Van Allen probes. *Journal of Geophysical Research: Space Physics*, *123*(5), 3704–3713. https://doi.org/10.1029/2017JA024782

Li, J., Bortnik, J., An, X., Li, W., Angelopoulos, V., Thorne, R. M., et al. (2019). Origin of two-band chorus in the radiation belt of Earth. *Nature Communications*, *10*(1), 4672. https://doi.org/10.1038/s41467-019-12561-3

Li, J., Bortnik, J., Li, W., An, X., Lyons, L. R., Kurth, W. S., et al. (2022). Unraveling the formation region and frequency of chorus spectral gaps. *Geophysical Research Letters*, *49*(19), e2022GL100385. https://doi.org/10.1029/2022GL100385

Liu, S., Gao, Z., Xiao, F., He, Q., Li, T., Shang, X., et al. (2021). Observation of unusual chorus elements by Van Allen probes. *Journal of Geophysical Research: Space Physics*, *126*(7), e2021JA029258. https://doi.org/10.1029/2021JA029258

McCollough, J. P., Miyoshi, Y., Ginet, G. P., Johnston, W. R., Su, Y.-J., Starks, M. J., et al. (2022). Space-to-space very low frequency radio transmission in the magnetosphere using the DSX and Arase satellites. *Earth Planets and Space*, *74*(1), 64. https://doi.org/10.1186/s40623-022-01605-6

Nogi, T., Nakamura, S., & Omura, Y. (2020). Full particle simulation of whistler-mode triggered falling-tone emissions in the magnetosphere. *Journal of Geophysical Research: Space Physics*, *125*(10), e2020JA027953. https://doi.org/10.1029/2020JA027953

Nogi, T., & Omura, Y. (2022). Nonlinear signatures of VLF-triggered emissions: A simulation study. *Journal of Geophysical Research: Space Physics*, *127*(1), e2021JA029826. https://doi.org/10.1029/2021JA029826

Nunn, D., & Omura, Y. (2012). A computational and theoretical analysis of falling frequency VLF emissions. *Journal of Geophysical Research: Space Physics*, *117*(A8), A08228. https://doi.org/10.1029/2012JA017557

Nunn, D., Zhang, X.-J., Mourenas, D., & Artemyev, A. V. (2021). Generation of realistic short chorus wave packets. *Geophysical Research Letters*, *48*(7), e2020GL092178. https://doi.org/10.1029/2020GL092178

Omura, Y. (2007). One-dimensional electromagnetic particle code KEMPO1: A tutorial on microphysics in space plasmas. In H. Usui, & Y. Omura (Eds.), *Advanced methods for space simulations* (pp. 1–21). Terra Scientific Publishing Company.

Omura, Y. (2021). Nonlinear wave growth theory of whistler-mode chorus and hiss emissions in the magnetosphere. *Earth Planets and Space*, *73*(1), 95. https://doi.org/10.1186/s40623-021-01380-w

Omura, Y., Hikishima, M., Katoh, Y., Summers, D., & Yagitani, S. (2009). Nonlinear mechanisms of lower-band and upper-band VLF chorus emissions in the magnetosphere. *Journal of Geophysical Research: Space Physics*, *114*(A7), A07217. https://doi.org/10.1029/2009JA014206

Omura, Y., Katoh, Y., & Summers, D. (2008). Theory and simulation of the generation of whistler-mode chorus. *Journal of Geophysical Research: Space Physics*, *113*(A4), A04223. https://doi.org/10.1029/2007JA012622

Omura, Y., & Matsumoto, H. (1993). KEMPO1: Technical guide to one-dimensional electromagnetic particle code. In H. Matsumoto, & Y. Omura (Eds.), *Computer space plasma physics: Simulation techniques and softwares* (pp. 21–65). Terra Scientific Publishing Company.

Omura, Y., & Nunn, D. (2011). Triggering process of whistler mode chorus emissions in the magnetosphere. *Journal of Geophysical Research: Space Physics*, *116*(A5), A05205. https://doi.org/10.1029/2010JA016280

Omura, Y., Nunn, D., Matsumoto, H., & Rycroft, M. (1991). A review of observational, theoretical and numerical studies of VLF triggered emissions. *Journal of Atmospheric and Terrestrial Physics*, *53*(5), 351–368. https://doi.org/10.1016/0021-9169(91)90031-2

Ratcliffe, H., & Watt, C. E. J. (2017). Self-consistent formation of a 0.5 cyclotron frequency gap in magnetospheric whistler mode waves. *Journal of Geophysical Research: Space Physics*, *122*(8), 8166–8180. https://doi.org/10.1002/2017JA024399

Reid, R. A., Marshall, R. A., Starks, M. J., Usanova, M. E., Wilson, G. R., Johnston, W. R., et al. (2022). Active VLF transmission experiments between the DSX and VPM spacecraft. *Journal of Geophysical Research: Space Physics*, *127*(4), e2021JA030087. https://doi.org/10.1029/2021JA030087

Roux, A., & Pellat, R. (1978). A theory of triggered emissions. *Journal of Geophysical Research: Space Physics*, *83*(A4), 1433–1441. https://doi.org/10.1029/JA083iA04p01433

Santolík, O., Kletzing, C. A., Kurth, W. S., Hospodarsky, G. B., & Bounds, S. R. (2014). Fine structure of large-amplitude chorus wave packets. *Geophysical Research Letters*, *41*(2), 293–299. https://doi.org/10.1002/2013GL058889

Sauer, K., Baumgärtel, K., & Sydora, R. (2020). Gap formation around $\Omega_e/2$ and generation of low-band whistler waves by landau-resonant electrons in the magnetosphere: Predictions from dispersion theory. *Earth and Planetary Physics*, *4*(2), 138–150. https://doi.org/10.26464/epp2020020

Shoji, M., & Omura, Y. (2013). Triggering process of electromagnetic ion cyclotron rising tone emissions in the inner magnetosphere. *Journal of Geophysical Research: Space Physics*, *118*(9), 5553–5561. https://doi.org/10.1002/jgra.50523

Tao, X., Zonca, F., & Chen, L. (2021). A "Trap-Release-Amplify"model of chorus waves. *Journal of Geophysical Research: Space Physics*, *126*(9), e2021JA029585. https://doi.org/10.1029/2021JA029585

Umeda, T., Omura, Y., & Matsumoto, H. (2001). An improved masking method for absorbing boundaries in electromagnetic particle simulations. *Computer Physics Communications*, *137*(2), 286–299. https://doi.org/10.1016/S0010-4655(01)00182-5

Zhang, X.-J., Demekhov, A. G., Katoh, Y., Nunn, D., Tao, X., Mourenas, D., et al. (2021). Fine structure of chorus wave packets: Comparison between observations and wave generation models. *Journal of Geophysical Research: Space Physics*, *126*(8), e2021JA029330. https://doi.org/10.1029/2021JA029330